Applied Catalysis B: Environment and Energy 346 (2024) 123779

Contents lists available at ScienceDirect

Applied Catalysis B: Environment and Energy

journal homepage: www.elsevier.com/locate/apcatb

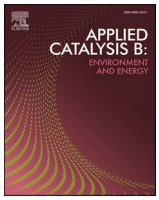

Single atomic Pt confined into lattice defect sites for low-temperature catalytic oxidation of VOCs

Fang Dong [a,1], Yu Meng [b,1], Weitong Ling [c], Weigao Han [a], Weiliang Han [a], Xiaona Li [c], Zhicheng Tang [a,*]

[a] State Key Laboratory for Oxo Synthesis and Selective Oxidation, National Engineering Research Center for Fine Petrochemical Intermediates, Lanzhou Institute of Chemical Physics, Chinese Academy of Sciences, Lanzhou 730000, PR China
[b] Shanxi Key Laboratory of Low Metamorphic Coal Clean Ytilization, School of Chemistry and Chemical Engineering, Yulin University, Yulin 719000, China
[c] State Key Laboratory of Fine Chemicals and Key Laboratory of Industrial Ecology and Environmental Engineering, School of Environmental Science & Technology, Dalian University of Technology, Dalian 116024, China

ARTICLE INFO

Keywords:
Pt single atom
CeO_2
MOFs
VOCs
Catalytic combustion

ABSTRACT

Development of low-cost noble Pt-based catalyst with superior catalytic performance is a challenge to achieve its application in VOCs catalytic oxidation. Although the single atom provides a strategy to design and develop highly efficient heterogeneous catalysts that simultaneously maximizes the utilization of precious metal atoms, the stability of single atom catalysts is not satisfactory as a result of its high atomic surface energy. Here we construct a $Pt_1@CeO_2$ single atom catalyst (SAC) with excellent catalytic activity for benzene catalytic combustion ($T_{90} = 212\ ^{\circ}C$) and low precious metal Pt loading, and even displaying an outstanding thermal stability and water resistance under the harsh conditions of 30,000 mL/g/h and 2000 ppm benzene. This $Pt_1@CeO_2$ catalyst was obtained by in situ domain limited encapsulation of Pt species in Ce-MOFs nanocages during the solvothermal reaction process. It is observed that lots of oxygen vacancies were created by the dislocation and phase transition of CeO_2 to provide abundant sites for anchoring single atomic Pt, which can be localized and anchored firmly to oxygen vacancies, thus forming the highly stable Pt single atom. The atomically dispersed Pt is capable of improving the catalytic activity by forming Pt-O band. The good water resistance may be ascribed to the confined Pt single atom into oxygen vacancies of CeO_2 support to form strong metal-support interaction (SMSI), and the PtO_x nanoparticles would be easy to aggregate deactivation under water vapor conditions. It is a simple and universal strategy to prepare Pt SAC via the inherently confined space of MOFs nanocages formed by coordination of organic ligands and metal ions, which benefits from the functional modification of ethylene glycol in MOFs self-assembly reaction.

1. Introduction

Heterogeneous catalysts for catalytic degradation of volatile organic compounds (VOCs) include transition metal oxide catalysts such as Co, Mn, Ce, Mg, Zr, Cu and Fe oxides [1–4], some structural oxides such as perovskite and spinel [5–7], and supported noble metal catalysts such as Pt, Pd, Rh and Ru-based catalysts [8–11]. Notably, Pt-based catalysts have received a lot of attention due to its excellent catalytic activity in VOCs catalytic combustion reaction. Unpleasantly, now Pt-based catalysts have high noble metal content and poor water resistance, which greatly limits their application in the industrial field. Therefore, the core and difficulty of VOCs catalytic combustion technology lies in reducing the loading of noble metal components, cutting its cost, and ensuring its excellent low temperature oxidation activity and stability.

As we all know, the catalytic activity of Pt, Pd, Rh and other noble metal catalysts chiefly depend on the size of noble metal nanoparticles, and the active species of noble metal with excellent catalytic performance exist usually in the formation of highly dispersed nanoclusters and single atom [12,13]. In other words, the catalytic activity of noble metal catalysts relies on the dispersion of active metal to a large extent, thus some efforts have been made to improve the low-temperature catalytic performance of catalysts through increasing the utilization

* Corresponding author.
E-mail address: tangzhicheng@licp.cas.cn (Z. Tang).
[1] These first authors contributed equally.

https://doi.org/10.1016/j.apcatb.2024.123779
Received 10 November 2023; Received in revised form 10 January 2024; Accepted 23 January 2024
Available online 26 January 2024

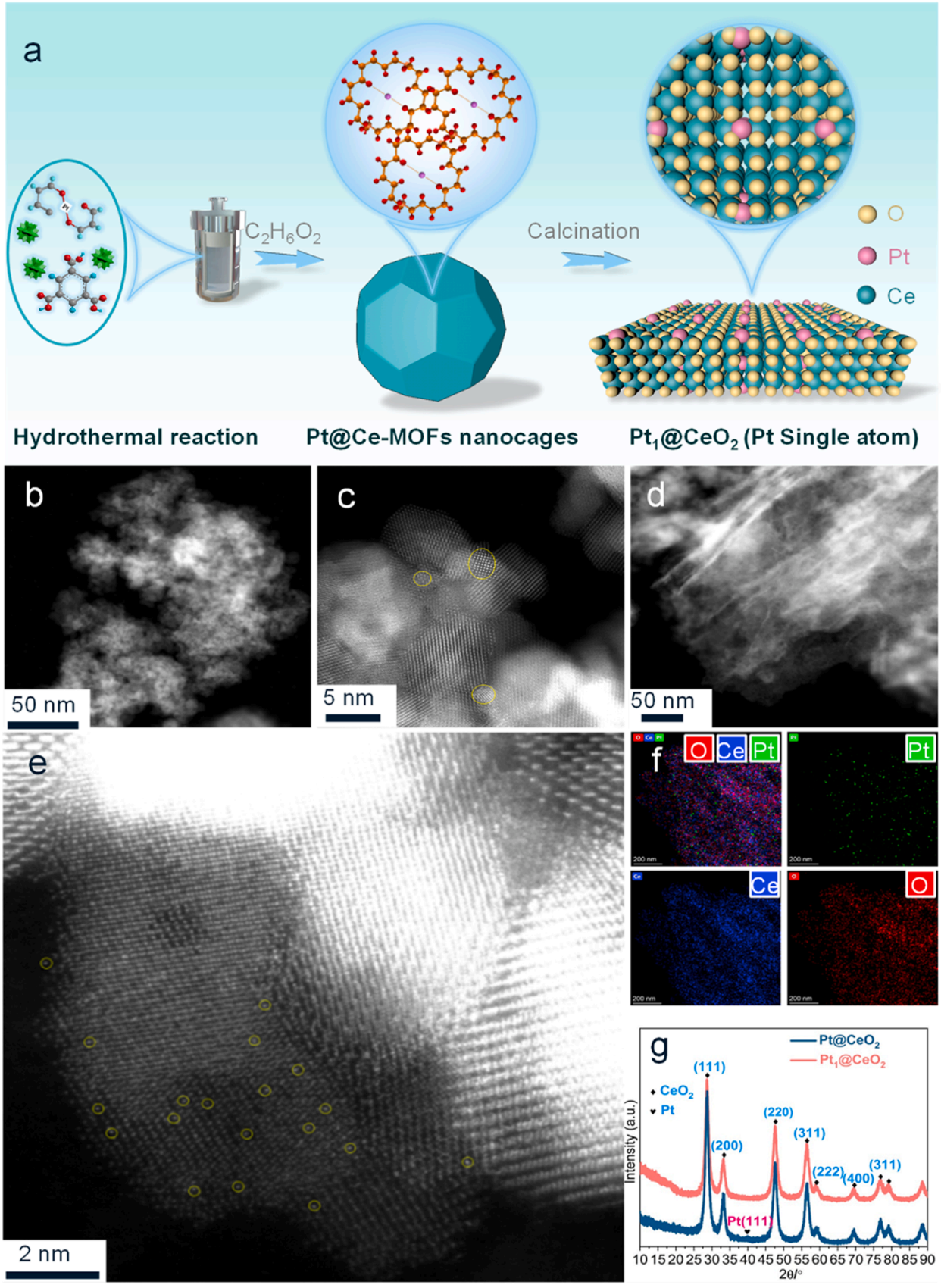

Fig. 1. Synthetic process and characterization of $Pt@CeO_2$ and $Pt_1@CeO_2$ samples: (a) Illustration of the synthesis of $Pt_1@CeO_2$, (b-e) The representative TEM image and Atomic resolution HAADF-STEM image of $Pt@CeO_2$ (b,c) and $Pt_1@CeO_2$ (d,e), Some of the Pt SAs are highlighted by yellow circles, (f) Corresponding EDS elemental maps of $Pt_1@CeO_2$ catalyst, and (g) XRD patterns of samples.

rate of noble metal atoms [14,15].

As described above, it is considered that the size of active metal plays a significant role in determining its catalytic activity, and the activation energy of reactant on the catalyst surface directly determines the level of the complete conversion temperature. Pt-based catalyst has been considered as the most promising precious metal catalyst. Zhang et. al found that PtW/Al_2O_3 showed the highest catalytic activity and the lowest activation energy for the catalytic combustion of benzene due to a Pt-MO_x (M =W, Mo) bimetallic synergistic effect [16]. The former work confirmed that the oxygen vacancies can be easily formed on the Pt SA/MgO, Pt/2Mn@NFO and $Pt_1Fe_{1.5}$/M surface, which facilitate the formation of active oxygen species [17–19]. In total, the dispersion of active metal is inversely proportional to the activation energy, and the higher dispersion of the active metal, the lower the activation energy of the reactant molecules [20,21]. It has been confirmed that the activation energy of single atom catalysts is orders of magnitude lower than that of nanoparticles and nanocluster catalysts, and the construction of single atom can achieve a highly efficient conversion of reactant molecules at low temperature [22].

Although SAC can improve greatly the utilization efficiency of precious metals, increase the reaction rate of reactant molecules, and deduce the reaction temperature, single atom tend to aggregate during the reaction process due to the high atomic surface energy [23,24]. The control of interaction between active metal and support is an extremely important tool to improve the thermal stability of single atom. Generally, the strong interaction of active metal and support can cause the rearrangement of electrons at their interface, and the extent and direction of charge transfer are driven by the difference between the Fermi energy levels of active metal and support, ultimately looking for an equilibrium of the electron chemical potential [25–27].

Herein, we propose the novel strategy to obtain a $Pt_1@CeO_2$ single atom catalyst (SAC) by in situ domain limited encapsulation of Pt species in Ce-MOFs nanocages. During the preparation process, the Pt species can be localized and anchored firmly to the defect sites of CeO_2, which come from the removal of lattice oxygen of CeO_2, thus achieving the formation of highly stable single atom Pt. For another, these forming oxygen vacancies can also accelerate the activation of oxygen molecules. The resulting $Pt_1@CeO_2$ single atom catalyst owned a low Pt loading, exhibited an excellent catalytic activity for the catalytic combustion of benzene and an outstanding water resistance. A series of characterizations indicate that the atomically dispersed Pt is capable of improving the catalytic activity by forming Pt-O band. We also observed that the good water resistance may be ascribed to the confined Pt single atom into oxygen vacancies of CeO_2 support, and the PtO_x nanoparticles would be easy to aggregate deactivation under water vapor conditions. In the presence of water, the formation of confined Pt single atom is the main reason for the excellent water resistant performance of $Pt_1@CeO_2$ catalyst. This strategy provides a new research perspective for the development of the hydrothermal stable Pt-based catalysts with low noble metal loading for wide industrial applications.

2. Methods

2.1. Chemicals and materials

Analytical grade ethylene glycol, N,N-Dimethylformamide (DMF), 2-amino-terephthalic acid, cerium nitrate hexahydrate were purchased from Shanghai Aladdin Reagent Co. Ltd, China. All chemicals were obtained from commercial supplier and used directly in this work without further purification.

2.2. Catalyst preparation

A certain quality $Pt(acac)_2$ was dissolved in the mixed solution of a mL ethylene glycol and b mL DMF for 20 min, and then 3.94 g 2-amino-terephthalic acid was added and continued for 20 min to form solution A. The 10.85 g $Ce(NO_3)_3{\cdot}6\ H_2O$ was also dissolved in the mixed solution of a mL ethylene glycol and b mL DMF with ultrasounding for 20 min, and persistently stirred to form solution B (a:b=0, 0.25, 0.50 and 0.75). After that, solution A is slowly poured into B transferred to the hydrothermal reactor at 120 °C for 24 h. Then centrifuge (10,000 rpm, 5 min), wash with DMF three times, vacuum drying at 90 °C for 12 h. After that, the product was roasted at 350 °C and the heating rate was 1 °C/min for 2 h. Finally, the resulting samples were respectively named as $Pt@CeO_2$, $Pt@CeO_2$-0.25, $Pt@CeO_2$-0.50 ($Pt_1@CeO_2$) and $Pt@CeO_2$-0.75 , in which the theoretical mass percentage of precious metal Pt is 0.5 %. In addition, the loading of Pt was also explored, and their preparation is the same with the $Pt@CeO_2$-0.50 ($Pt_1@CeO_2$) sample. The obtained samples were marked as 0.1 %$Pt@CeO_2$, 0.3 %$Pt@CeO_2$, and 0.7 %$Pt@CeO_2$. Furthermore, the preparation process of reference CeO_2 sample was consistent with that of the $Pt@CeO_2$-0.50 sample.

2.3. Catalytic performance test

The test was conducted on a continuous flow micro-reactor (8 mm of inner diameter, length of 30 cm). The error of carbon balance is about ±3 %, and the specific calculation process has been listed in the Supporting information.

2.4. Catalyst characterization

The microstructure of the precursors and samples was verified by a Transmission electron microscopy (TEM) analysis. TEM image was carried out on a JEOL JEM-2010 transmission electron microscope equipped with an Oxford energy dispersive X-ray (EDX) spectrometer attachment operating at 200 kV. For TEM analysis, the samples were dispersed uniformly in the ethanol solution, which were in further installed on double sided adhesive tape. The specific information of other characterizations is listed in Supporting Information.

2.5. Computing method

Density functional theory (DFT) calculation was conducted on the surface of single atom Pt_1 $@CeO_2$ catalyst. The density functional theory (DFT) method employed the VASP package with PBE+U (U_{eff}=5.0 eV) approximation.

3. Results and discussion

3.1. Characterization of single atom Pt confined into oxygen defect sites of CeO_2

In a typical process, the ethylene glycol was used as reducing agent to produce oxygen vacancies, which can anchor Pt species and form a series of stable Pt single atom on the CeO_2 substrate. Besides, oxygen vacancies can promote the activation of oxygen molecules to produce lots of active oxygen species and accelerate the catalytic combustion of benzene. The synthesis process of single atom $Pt_1@CeO_2$ catalyst is shown in Fig. 1a. Concretely, we had prepared various $Pt@CeO_2$ catalysts treated with different amounts of reducing agents, including the $Pt@CeO_2$-0.25, $Pt@CeO_2$-0.50 ($Pt_1@CeO_2$) and $Pt@CeO_2$-0.75 samples, in which the volume ratio of ethylene glycol (reducing agent) and solvent DMF was respectively 0.25, 0.50 and 0.75. A reference $Pt@CeO_2$ catalyst was also prepared by the same method process without adding the reducing agents. Furthermore, the High-angle annular dark-field imaging scanning transmission electron microscopy (HAADF-STEM) was conducted to explore the dispersion of Pt species. We observed a large number of homogeneously distributed Pt nanocluster and nanoparticles (NPs) with diameters of ~1 nm in the Pt nanocluster and diameters of ~ 2 nm in the Pt NPs on $Pt@CeO_2$ sample (Fig. 1b and c). On the contrary, the HAADF-STEM results of the $Pt_1@CeO_2$ sample verified the presence of a lot of Pt single atoms with diameters of ~0.1 nm in

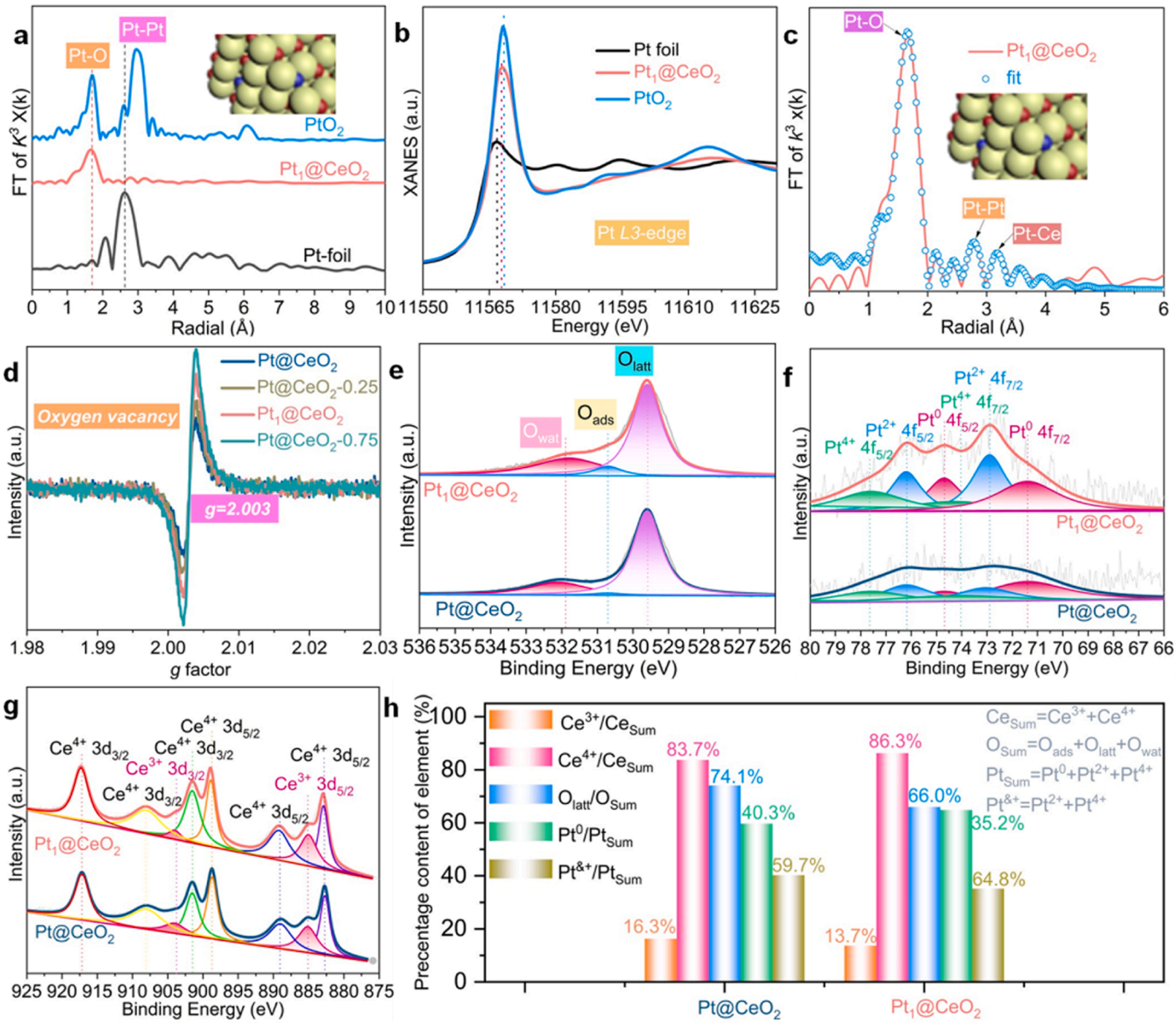

Fig. 2. The k_3-weighted Fourier transform FT-EXAFS spectra (Pt L_3-edge) of PtO_2, $Pt_1@CeO_2$ and Pt foil (a), the Pt L_3-edge XANES of PtO_2, $Pt_1@CeO_2$ and Pt foil (b), Fitting of the FT-EXAFS curve of $Pt_1@CeO_2$ sample (c), Corresponding electron factor by Low-temperature EPR spectra of magnetic field of $Pt@CeO_2$, $Pt@CeO_2$-0.25, $Pt_1@CeO_2$ ($Pt@CeO_2$-0.50) and $Pt@CeO_2$-0.75 samples (d), O 1s XPS spectra (e), Pt 4f XPS spectra (f), Ce 3d XPS spectra (g), and the percentage content of different species (h) on the surface of $Pt@CeO_2$ and $Pt_1@CeO_2$ samples.

Fig. 1d and e. In addition, energy-dispersive X-ray spectroscopy (EDS) elemental mapping of $Pt_1@CeO_2$ sample confirmed a uniform distribution of Pt atom over the CeO_2 support (Fig. 1f). X-ray diffraction patterns (XRD) of $Pt_1@CeO_2$ sample (Fig. 1g) did not show any Pt-containing crystal phase as a result of the presence of very small Pt single atoms. On the contrary, the XRD of $Pt@CeO_2$ sample shows an obvious diffraction peak of Pt (111) crystal phases, indicating the existence of large grain Pt species.

To verify further the existence of only atomically dispersed individual Pt atom over $Pt_1@CeO_2$ sample, extended X-ray absorption fine structure (EXAFS) spectra were conducted on the fresh $Pt_1@CeO_2$ sample in Fig. 2a. Correspondingly, in the Fourier transforms of the EXAFS data, one distinct peak at 1.7 Å was ascribed to the contribution of Pt-O species, and a very weak peak at 2.8 Å was assigned to the contribution of Pt-Pt. As a result of the disordering in the high level layer, there has only the one main peak in the range of 1.0–4.0 Å, which need to be conducted in the EXAFS curve-fitting, and the fitting results are listed in Table S1. The peak at a distance of 1.73 Å was related to the contribution of Pt-O band for the $Pt_1@CeO_2$ sample, and their coordination number was around 3.7. It is considered that the Pt-O coordination was most probably related to the interaction between Pt and the CeO_x support [28]. The bonding distance of Pt-O is close to that of PtO_2, suggesting the formation of strong metal-support interaction. For Pt foil, the peak at a distance of 2.75 Å was ascribed to the Pt-Pt contribution in Fig. S1, and their average coordination number is 12. Compared with Pt foil, it is observed that the Pt-Pt bonding coordination number of $Pt_1@CeO_2$ sample is much lower than that of Pt foil, and the Pt-Pt bonding is not present in the second shell of the $Pt_1@CeO_2$ sample. As the Pt's closest neighbours are O atoms, the Pt-Ce coordination dates from the next-closest neighbour Ce, which was bridged by the nearest O atom. The EXAFS results do not display any contributions of Pt-Pt and Pt-Ce bonding over the $Pt_1@CeO_2$ sample, in keeping with the HAADF result that the Pt species of $Pt_1@CeO_2$ sample exists only the formation of Pt single atoms.

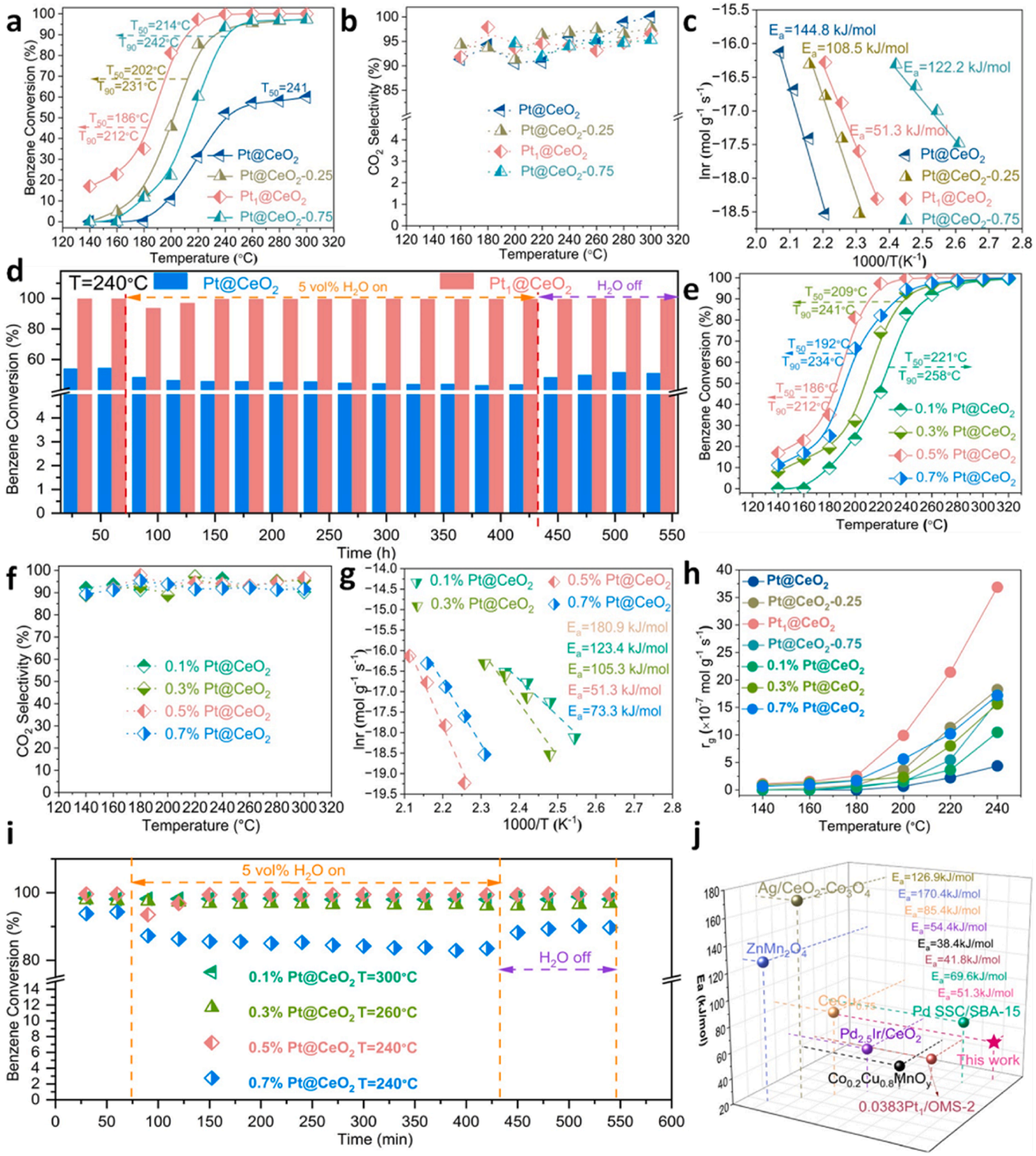

Fig. 3. The catalytic performance of these Pt@CeO_2 catalysts: Effect of reducing agent on (a) benzene conversion, (b) CO_2 selectivity, (c) Arrhenius plots as a function of reaction temperature, (d) Water resistance; Effect of Pt loading on (e) benzene conversion, (f) CO_2 selectivity, (g) Arrhenius plots as a function of reaction temperature. (h) Reaction rates on basis of the catalyst mass, (i) Water resistance of x%Pt@CeO_2 catalysts, and Fig. 3j. Activation energy of Pt_1 @CeO_2 catalyst and that of other reported catalysts.

Fig. 2b shows the normalized X-ray absorption near-edge structure (XANES) spectra of the Pt_1@CeO_2 sample, and the reference spectra of Pt foil and PtO_2. It is observed that the absorption edge of Pt foil was located at 11,567.5 eV, the adsorption edge of PtO_2 occurred at 11,568.5 eV, and the adsorption edge of Pt_1@CeO_2 exhibited at 11,568.1 eV. The XANES spectra of Pt L3-edge further demonstrated that the average valence state of Pt species in the Pt_1@CeO_2 catalyst is between Pt^0 and Pt^{4+}, as verified by the absorption edge of Pt_1@CeO_2 situated between Pt foil and PtO_2. The results confirmed that the intensity of Pt_1@CeO_2 is between that of Pt foil and PtO_2, further

indicating that the Pt single atoms were formed [29]. The fitting analysis (Fig. 2c) expressly confirmed that in $Pt_1@CeO_2$ sample each Pt atom is coordinated by four O atoms following an average bond length of 2.03 Å (Table S1). The above results verified that the Pt atoms of $Pt_1@CeO_2$ sample are atomically dispersed, which is accordance with the HADDF-STEM results (Fig. 1).

To further explore the formation of oxygen vacancies (O_v), the low-temperature EPR analysis were conducted and shown in Fig. 2d and Fig. S4. The corresponding electron factor (ca. 2.003) and obvious magnetic field signal (ca. 3515 G) reveal the presence of typical O_v in these $Pt@CeO_2$ catalysts [30,31]. Moreover, the quantitative results illustrate that the addition of reducing agent can promote the formation of a large number of oxygen vacancies. Among these samples, the $Pt@CeO_2$-0.75 catalyst acquires the highest concentration of oxygen vacancies. It is inferred that a large number oxygen vacancies were created by the dislocation and phase transition of CeO_2. More importantly, these forming oxygen vacancies can provide abundant sites for the anchoring of highly dispersed Pt atoms.

To investigate the effect of reducing agent on the chemical valence state of elements, the X-ray photoelectron spectroscopy (XPS) measurements were executed on these samples (Fig. 2e–g). The O1s XPS was conducted in Fig. 2e, we observed that there are three peaks in the form of lattice oxygen (O_{latt}), adsorbed oxygen (O_{ads}) and adsorbed water (O_{wat}). The fitting results of O 1s XPS verified that the content of O_{latt} is in order of $Pt@CeO_2$ (74.05 %) > $Pt_1@CeO_2$ (66.04 %), indicating fully that the addition of reducing agent led to the removal of part lattice oxygen. In other words, the more oxygen vacancies were formed on the surface of $Pt_1@CeO_2$ sample, and the results were consistent with the EPR results.

The Pt 4f spectra were fitted into six peaks, including Pt^{4+} $4f_{5/2}$ at 77.6 eV, Pt^{2+} $4f_{5/2}$ at 76.2 eV, Pt^0 4 $f_{5/2}$ at 74.7 eV, Pt^{4+} $4f_{7/2}$ at 74.3 eV, Pt^{2+} $4f_{7/2}$ at 72.9 eV and Pt^0 $4f_{7/2}$ at 71.4 eV in Fig. 2f. It is observed that the ratio of Pt^0/Pt_{sum} over $Pt@CeO_2$ catalyst is 40.28 %, and the value of Pt^0/Pt_{sum} ratio over $Pt_1@CeO_2$ sample is 35.16 %. Through evaluating the ratio of different Pt species, it is confirmed that the Pt species over these catalysts mainly exists in the formation of Pt^{2+} and Pt^{4+} species, and the relative of Pt^{2+} and Pt^{4+} species has been also listed in Table S5. Simultaneously, it is also discovered that the content of Pt^0 species decreased significantly over the $Pt_1@CeO_2$ sample surface, indicating that the reducing agents could not cause the completed reduction of surface precious metal $Pt^{\&+}$ species. The Ce 3d XPS results were shown in Fig. 2g, and it is discovered that the Ce 3d spectra appear the existence of eight peaks corresponding to $3d_{3/2}$ and $3d_{5/2}$ spin-obit components [32,33]. The ratio of surface Ce^{4+}/Ce_{sum} are also listed in Table S5. The ratio of Ce^{4+}/Ce_{sum} over the $Pt_1@CeO_2$ sample is 86.34 %, while that of the $Pt@CeO_2$ sample is 83.65 %. We observed that the ratio of Ce^{4+}/Ce_{sum} over the $Pt_1@CeO_2$ sample was very close. For another, the ratio of Pt and Ce was also analyzed, and the higher Pt/Ce ratio over $Pt_1@CeO_2$ indicates the existence of highly dispersed Pt species, in according with the HAADF-STEM results. Analogously, the Raman, XRD and XPS characterizations of the $Pt@CeO_2$-0.25 and $Pt@CeO_2$-0.75 samples also conducted and exhibited in Fig. S5-9. These results fully indicate that the addition of reducing agent is extremely beneficial to the formation and anchoring of stable monatomic Pt.

3.2. Catalytic performance

To verify the key role of oxygen vacancies in anchoring single atom Pt, the loading of precious metal was also investigated in detail. Herein, a series of x%$Pt@CeO_2$ samples with different Pt loading were prepared through the same synthesized method with $Pt_1@CeO_2$ sample. Concretely, the x%$Pt@CeO_2$ samples were prepared by a modified solvothermal method, in which ethylene glycol was used to form oxygen vacancies in an autoclave, and the volume ratio of ethylene glycol and DMF was still 0.50. On this basis, we chose benzene oxidation as probe to explore the catalytic performance of these $Pt@CeO_2$ catalysts. Fig. 3 exhibited the catalytic performance of these $Pt@CeO_2$ catalysts, including the effect of reducing agent and Pt loadings on their catalytic performance. For Fig. 3a, it is discovered that when the volume ratio of ethylene glycol and DMF was 0.50, the $Pt@CeO_2$ catalyst exhibited the best catalytic activity for benzene catalytic oxidation. The T_{50} of $Pt@CeO_2$, $Pt@CeO_2$-0.25, $Pt@CeO_2$-0.50 ($Pt_1@CeO_2$) and $Pt@CeO_2$-0.75 samples are respectively 241 °C, 202 °C, 186 °C and 214 °C, and the T_{90} of $Pt@CeO_2$-0.25, $Pt@CeO_2$-0.50 (Pt_1 $@CeO_2$) and $Pt@CeO_2$-0.75 samples are respectively 231 °C, 212 °C, and 242 °C. We observed that the adding of reducing agent improved significantly the activity of $Pt@CeO_2$ catalysts, while the excessive addition of reducing agent decreased unfortunately the catalytic activity. The selectivity of the products CO_2 was also conducted and listed in Fig. 3b. The activation energy (E_a) of these catalysts is calculated to evaluate their performance, and the results in Fig. 3c confirmed that the $Pt_1@CeO_2$ catalyst owned the lowest E_a value. Furthermore, the water resistance of $Pt@CeO_2$ and $Pt_1@CeO_2$ samples was probed and exhibited in Fig. 3d, and we observed that the $Pt_1@CeO_2$ sample exhibited an excellent water resistance during reaction process. However, the $Pt@CeO_2$ catalyst appeared the decline of benzene conversion under water vapor conditions. After the water was stopped, the conversion rate of benzene increased slightly over the $Pt@CeO_2$ catalyst, indicating that in addition to the competitive adsorption of water and reactant on the catalyst surface, there may be also irreversible inactivation of active species over the $Pt@CeO_2$ catalyst. The irreversible inactivation of active species over the $Pt@CeO_2$ catalyst might be caused by intermediate productions and the aggregation of active centers.

For Fig. 3e, the activity results verified that the 0.5 %$Pt@CeO_2$ ($Pt_1@CeO_2$) catalyst owned the best activity for benzene catalytic oxidation, and the reasons were related to the exposed area of active Pt species. The T_{50} and T_{90} of 0.1 %$Pt@CeO_2$, 0.3 %$Pt@CeO_2$, 0.5 % $Pt@CeO_2$ ($Pt_1@CeO_2$) and 0.7 %$Pt@CeO_2$ samples are respectively 221 °C and 258 °C, 209 °C and 241 °C, 186 °C and 212 °C, 192 °C and 234 °C. Among these samples, we observed that the 0.5 %$Pt@CeO_2$ sample owns the lowest T_{50} and T_{90}, indicating its best catalytic activity. The Fig. 3f is assigned to the selectivity of CO_2, and it is discovered that the CO_2 is the main products of benzene catalytic combustion. To avoid the effect of heat generated by the reaction itself, we calculated the activation energy (E_a) of these samples under the condition that the conversion of benzene is less than 15 %. The results were listed in Fig. 3g, it is confirmed that the 0.5 %$Pt@CeO_2$ catalyst owned the lowest E_a value, and the order of E_a value is 0.5 %$Pt@CeO_2$ (51.3 kJ/mol) < 0.7 %$Pt@CeO_2$ (73.3 kJ/mol) < 0.3 %$Pt@CeO_2$ (105.3 kJ/mol) < 0.1 % $Pt@CeO_2$ (123.4 kJ/mol). For benzene oxidation, the $Pt_1@CeO_2$ catalyst gave a mass reaction rate of 21.41×10^{-7} mol g^{-1} s^{-1} at the reaction temperature of 220 °C, which is about 10 times that of $Pt@CeO_2$ in Fig. 3h.

The mass reaction rate of $Pt@CeO_2$-0.25, $Pt@CeO_2$-0.75, 0.1 % $Pt@CeO_2$, 0.3 %$Pt@CeO_2$ and 0.7 %$Pt@CeO_2$ catalysts were also higher than that of $Pt@CeO_2$ catalysts, and the $Pt_1@CeO_2$ sample was 2–7 times as active as the other three samples. Meanwhile, the surface reaction rate of catalyst is also calculated based on the specific surface area of catalysts (Fig. S10). Among these catalysts, the single atom $Pt_1@CeO_2$ catalyst exhibited the best catalytic activity. The above results confirmed that the addition of reducing agent does significantly increase the reaction rate of catalyst, reduce the activation energy, and realize the complete catalytic oxidation of benzene at a lower temperature. The water resistant of these x %$Pt@CeO_2$ catalysts were also evaluated and shown in Fig. 3i, and we observed that the 0.1 %$Pt@CeO_2$, 0.3 % $Pt@CeO_2$ and 0.5 %$Pt@CeO_2$ catalysts all show good water resistance, and only the 0.7 %$Pt@CeO_2$ catalyst shows a slight decrease in benzene conversion under humid conditions. The reasons may be related to the appearance of few isolated Pt and PtO_x species on the surface of 0.7 % $Pt@CeO_2$ catalyst during reaction process. Compared with the existing literatures [16–19, 34–40], it is verified that the $Pt_1@CeO_2$ catalyst prepared by the limited encapsulation strategy owns a relatively

Table 1
The catalytic performance of the former literatures.

Catalysts	Reaction conditions	T_{50}	T_{90}	Refs
PtW/Al_2O_3	40,000 mL/(g·h); 1000 ppm benzene	133	140	15
0.5Pt/EG	36,000 mL/(g·h), 100 ppm toluene	160	220	16
2 %Pt/2Mn@NFO	36 000 mL/(g·h), 50 ppm toluene	107	113	17
$PtSn/CeO_2$	40,000 mL/(g·h), 1000 ppm toluene	270	310	18
$Pt_1Fe_{0.79}/M$	40,000 mL/(g·h), 1000 ppm toluene	175	186	19
$Pt_1@CeO_2$	30,000 mL/(g·h), 2000 ppm benzene	186	212	This work

excellent low temperature oxidation activity in Fig. 3j, Table 1and Fig. S11.

3.3. Effect of Pt loading on the texture and chemical state of single atom Pt

The Pt loading also played an important role in controlling the catalytic activity, microstructure and electronic properties of $Pt@CeO_2$ catalysts. To probe the effect of structure and chemical states on the catalytic performance, various characterizations were conducted. XRD patterns in Fig. 4a confirm that the calcined CeO_2 support and x% $Pt@CeO_2$ samples have the cubic fluorite structure of CeO_2. No diffraction peak of Pt was observed over 0.1 $\%Pt@CeO_2$, 0.3 $\%Pt@CeO_2$ and 0.5 $\%Pt@CeO_2$ catalysts, while there has an obvious diffraction peak of Pt(111) over 0.7 $\%Pt@CeO_2$ catalyst. The results of XRD verified that there are no diffraction peak of Pt species over 0.1 $\%Pt@CeO_2$ and 0.3 $\%Pt@CeO_2$ catalysts due to low precious metal content. The Pt species over 0.5 $\%Pt@CeO_2$ catalyst were highly dispersed, indicating that the Pt species exist as a highly dispersed state. Raman spectra of

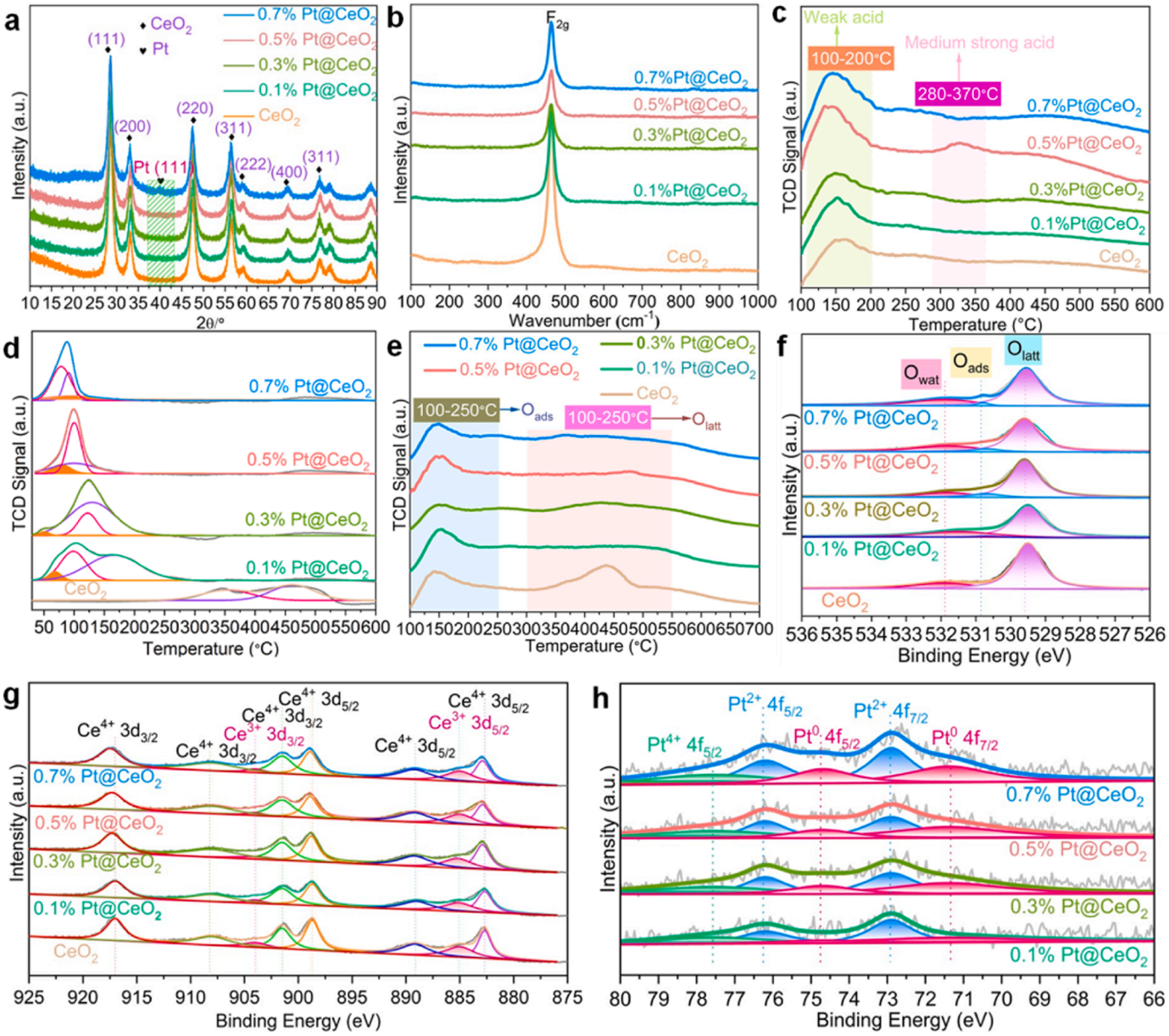

Fig. 4. XRD (a), Raman (b), NH_3-TPD (c), H_2-TPR (d), O_2-TPD (e), O 1s XPS (f), Ce 3d XPS (g), Pt 4f XPS (h) results of x $\%Pt@CeO_2$ catalysts.

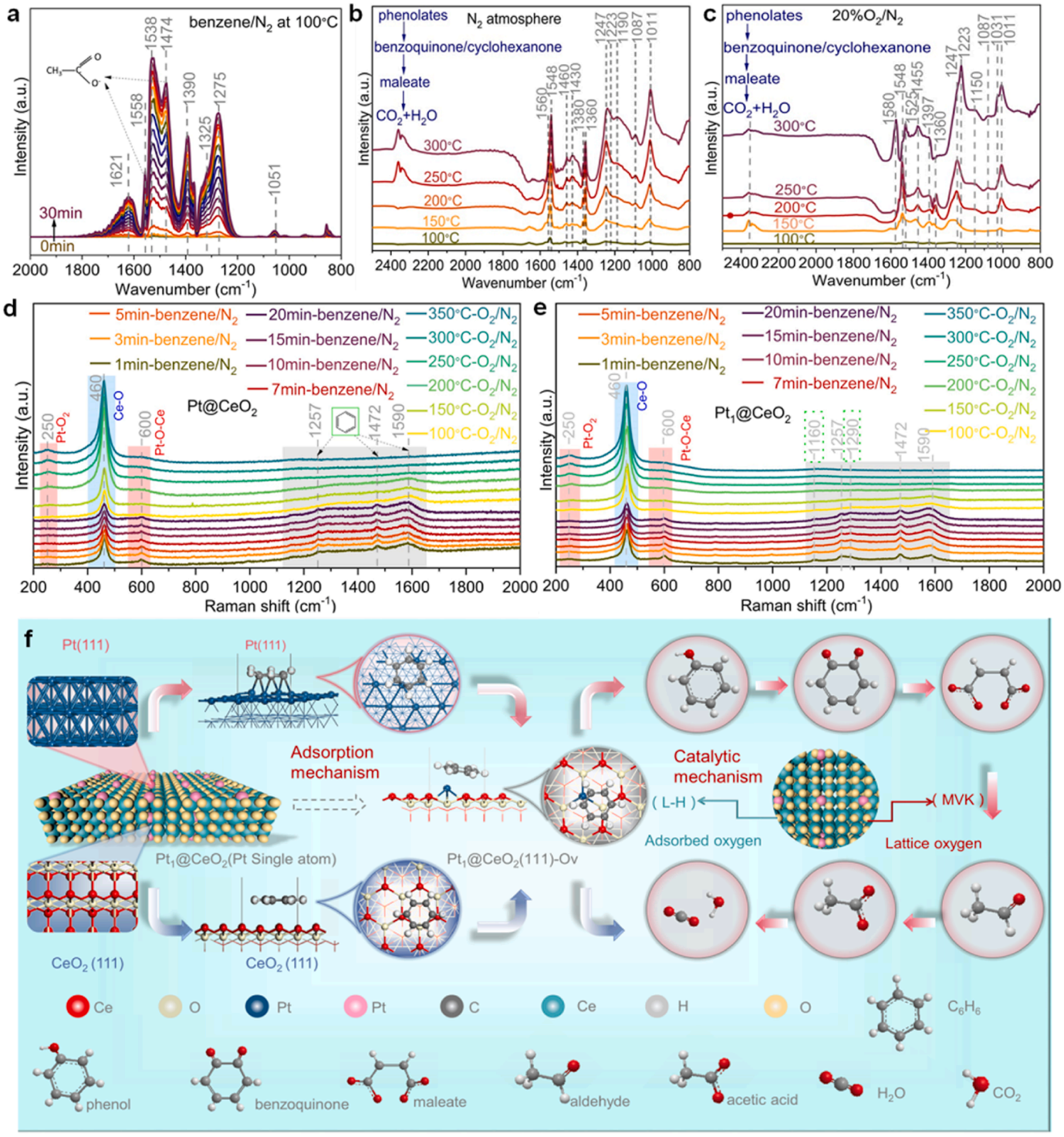

Fig. 5. In situ DRIFTS of Pt_1 @CeO_2 catalyst: (a) the adsorption process of benzene at 100 °C, (b) the spectra of benzene desorption at different temperature under N_2 flow of 25 mL/min, (c) the spectra of benzene desorption at different temperature under 20 vol% O_2/N_2 flow of 25 mL/min; In situ SERS of Pt@CeO_2 catalyst (d), and in situ SERS of Pt_1 @CeO_2 catalyst (e) under N_2 and 20 vol% O_2/N_2 atmosphere, respectively. (f) The adsorption of benzene on the surface of Pt, CeO_2 and Pt_1 @CeO_2 and the reaction pathways of benzene catalytic oxidation over Pt_1 @CeO_2 catalyst.

these samples were conducted in Fig. 4b, and a prominent band at 460 cm^{-1} was attributed to the F_{2g} mode of CeO_2 with the fluorite structure. With the addition of Pt species, this peak become weak and broad, which can be attributed to the contribution of Pt-O-Ce and Pt-O-Pt bonds in these Pt@CeO_2 catalysts. Acidity of samples is also vital for the adsorption of benzene molecular, and the NH_3-TPD experiments were conducted to explore the acidity in Fig. 4c. Accordingly, these peaks were divided into two regions: (1) the peak at 100–200 °C was ascribed to the desorption of NH_3 molecular from weak acid sites; (2) the peak at 280–370 °C was related to the desorption of NH_3 molecular from medium strong acid. It is discovered that all samples showed the desorption peak at 100–200 °C. Only 0.5 %Pt@CeO_2 sample exhibited the desorption peak at 280–370 °C, which was assigned to the contribution of medium strong acid [41,42]. The above results fully confirmed

that the medium strong acid may be more conducive to promoting the adsorption and transformation of benzene molecules. H_2-TPR results in Fig. 4d confirmed that the addition of Pt species decreased obviously the reduction temperature of CeO_2, and the reduction temperature of Pt@CeO_2 catalyst decreased significantly with the increase of Pt content. For pure CeO_2, a broad peak was observed in the range of 270–550 °C, indicating the reduction of surface oxygen species. However, these Pt@CeO_2 samples appear an obvious decrease in reduction temperature. This phenomenon is probably related to the existence of Pt-O-Ce interaction. H_2 molecules are preferentially activated at the precious metal Pt site, and the forming active hydrogen spills onto CeO_2 surface and rapidly reduces the surface lattice oxygen of CeO_2 at low temperature [43,44]. The higher the Pt content, the more Pt-O-Ce bonds are formed. Therefore, the activation rate of lattice oxygen increases with the increase of Pt content, and their reduction temperature decrease increasingly.

O_2-TPD experiment (Fig. 4e) was used to verify the difference of oxygen species over these Pt@CeO_2 catalysts. Interestingly, we observed that the content of lattice oxygen (O_{latt}) in CeO_2 is highest, and the addition of Pt species decreased obviously the content of O_{latt}. During the preparation process, the reducing agent causes the removal of lattice oxygen, forming a large number of oxygen vacancies, and then the precious metal Pt is anchored to the oxygen vacancy in the formation of single atomic Pt. As we all know, the oxygen vacancy (O_v) is a kind of point defect of metal oxides, which can be treated as an anchoring site to confine metal ions [45,46]. Contrast with Pt nanoparticles, single atom Pt can improve greatly the adsorption and activation of oxygen molecules, thus increasing its catalytic performance [9,35].

XPS characterizations were also executed to explore the chemical states of O species, Pt species and Ce species over theses x %Pt@CeO_2 catalysts. O1s XPS of these x %Pt@CeO_2 catalysts were conducted and listed in Fig. 4f, we observed that there are three peaks in the form of lattice oxygen (O_{latt}), adsorbed oxygen (O_{ads}) and adsorbed water (O_{wat}). The fitting results of O 1s XPS verified that the content of O_{latt} is in order of CeO_2 (78.65) > 0.7 %Pt@CeO_2 (70.66 %) > 0.3 %Pt@CeO_2 (67.14 % > 0.5 %Pt@CeO_2 (66.05 %) > 0.1 %Pt@CeO_2 (48.42 %), indicating that the loading of Pt decreased obviously the number of lattice oxygen due to the use of reducing agents during loading Pt process. The removal of lattice oxygen would be good for the formation of oxygen vacancies, which provides extremely favorable conditions for anchoring single atomic Pt. The results were consistent with the O_2-TPD results. The Ce 3d XPS results were shown in Fig. 4g, and it is discovered that the Ce 3d spectra appear the existence of eight peaks corresponding to $3d_{3/2}$ and $3d_{5/2}$ spin-obit components. The ratio of surface Ce^{4+}/Ce_{sum} are also listed in Table S9. The reducing agent could strip the lattice oxygen of CeO_2 to form some oxygen vacancies, which could anchor the noble active Pt species and improve the dispersion of Pt species. It is confirmed that the ratio of Ce^{4+}/Ce_{sum} is 85.79, 85.74, 86.34 and 85.87 over the 0.1 %Pt@CeO_2, 0.3 %Pt@CeO_2, 0.5 % Pt@CeO_2 and 0.7 %Pt@CeO_2 catalysts. The ratio of Ce^{4+}/Ce_{sum} over these Pt@CeO_2 sample was very close. On the one hand, the reduce agent mainly plays the role for forming the oxygen vacancy through stripping the lattice oxygen of CeO_2. On the other hand, the reduce agent might change the chemical state of Pt species. It is noting that the strong interaction of metal and support could change the chemical state of Ce and Pt species. The difference of Ce^{4+}/Ce^{3+} ratio is related to the formation of oxygen vacancies, the interaction of Pt and CeO_2, the charge transfer between precious metals Pt and Ce species and so on.

The Pt 4f spectra are conducted to probe the surface content and chemical state of Pt over these catalysts. Accordingly, Pt 4f spectra were fitted into six peaks, including Pt^{4+} $4f_{5/2}$ at 77.6 eV, Pt^{2+} $4f_{5/2}$ at 76.2 eV, Pt^0 $4f_{5/2}$ at 74.7 eV, Pt^{4+} $4f_{7/2}$ at 74.3 eV, Pt^{2+} $4f_{7/2}$ at 72.9 eV and Pt^0 $4f_{7/2}$ at 71.4 eV in Fig. 4h. It is observed in Table S9 that the ratio of Pt^0/Pt_{sum} over 0.5 %Pt@CeO_2 catalyst is highest, and the order of Pt^0/Pt_{sum} ratio is 0.5 %Pt@CeO_2 (35.16 %) > 0.3 %Pt@CeO_2 (34.24 %) > 0.1 %Pt@CeO_2 (33.70 %) > 0.7 %Pt@CeO_2 (30.60 %). Through evaluating the ratio of Pt species, it is confirmed that the Pt species over these catalysts mainly exists in the formation of Pt^{2+} and Pt^{4+} species, and the results were listed in Table S9. Combined with the activity results, it is concluded that the Pt^0 species may play an important role in the activation of oxygen molecules [7,17].

The specific surface area of these catalysts was measured by N_2 physisorption characterization, and the S_{BET} of CeO_2, 0.1 %Pt@CeO_2, 0.3 %Pt@CeO_2, 0.5 %Pt@CeO_2 and 0.7 %Pt@CeO_2 samples are 94.70 m^2/g, 97.50 m^2/g, 91.01 m^2/g, 90.09 m^2/g and 82.49 m^2/g, respectively (Table S10). The high porosity is vitally significant for increasing the diffusion rate of reactants and products, generating favorable catalytic kinetics (Table S10 and Fig. S12). In addition, it is found that the overall Pt content in these x%Pt@CeO_2 catalysts was decided by inductively coupled plasma optical emission spectrometry (ICP-OES) in Table S10. Combined with the above analysis, it is confirmed that the oxygen vacancies derived from the removal of lattice oxygen of CeO_x support can be filled by highly dispersed Pt species, and the electron transfer appeared from Pt to CeO_x and restricted the aggregation of Pt species during thermal treatment and reaction process. The Pt species was uniformly dispersed and anchored in CeO_x to create high efficiency single atom Pt sites and unsaturated Pt species, and the addition of ethylene glycol promoted the anchoring of highly dispersed Pt sites adjacent to oxygen vacancies of CeO_x.

3.4. The role of reactive oxygen species and density functional theory studies

To investigate the formation of intermediates to put forward a reasonable reaction pathway, in situ DRIFTS were conducted on the Pt@CeO_2 and Pt_1@CeO_2 catalysts. The process was conducted in the N_2 and 20 vol% O_2/N_2 atmospheres to understand thoroughly the effect of lattice oxygen and adsorbed oxygen species. Fig. 5a shows in situ DRIFTS spectra of Pt_1@CeO_2 catalyst in the presence of benzene/N_2 at different times. A series of characteristic absorbance bands of benzene over the surface of Pt_1@CeO_2 sample were clearly detected. The bands at 1051 cm^{-1} were related to the C-H deformation vibrations, and the weak band at 1325 cm^{-1} was due to the ring vibrations of benzene. The band at 1572 cm^{-1} could be assigned to the C=C stretching vibrations of the phenolate species. The strong band at 1558 cm^{-1} was attributed to the asymmetric -COO- stretching vibration, and the band at 1474 cm^{-1} was the symmetric -COO- stretching vibration [47,48]. The peak at 1538 cm^{-1} was attributed to the maleate species. The peaks at 1621 cm^{-1} was assigned to the typical region of carbonyl stretching. The above phenomenon indicated that benzene was first oxidized into phenolates, the formed phenolates were then transformed into benzoquinone. Interestingly, it is discovered that various intermediates have formed during the adsorption process of benzene, indicating the lattice oxygen participated in the reaction during the adsorption process at low temperature. The increase of reaction temperature under N_2 atmosphere in Fig. 5b could promote the formation of maleate, aldehyde and acetate species. We observed these intermediates cannot be fully converted into the final products CO_2 and H_2O in N_2 atmosphere even at 250 °C. On the contrary, the use of 20 vol%O_2/N_2 can accelerate the conversion of these intermediates at low temperatures, and a large number of H_2O characteristic peaks were detected at even 150 °C in Fig. 5c. The above phenomenon indicate that the catalytic oxidation of benzene over the Pt_1@CeO_2 catalyst is dominated by MvK (Mars-van Krevelen) mechanism involving lattice oxygen at low temperature, and at high temperature L-H (Langmuir-Hinshelwood) mechanism played a key role involving adsorbed oxygen. In comparison, in situ DRIFTS of Pt@CeO_2 catalyst was also conducted in the N_2 and 20 vol% O_2/N_2 atmospheres, and the results were listed in Fig. S13-15. On basis of in situ DRIFTS results, it is considered that the phenol, benzoquinone, maleate, aldehyde, acetate species are the main intermediates over Pt_1@CeO_2 catalyst. It is speculated that benzene was first converted into phenolates with the help of active oxygen species, and the formed phenol were then

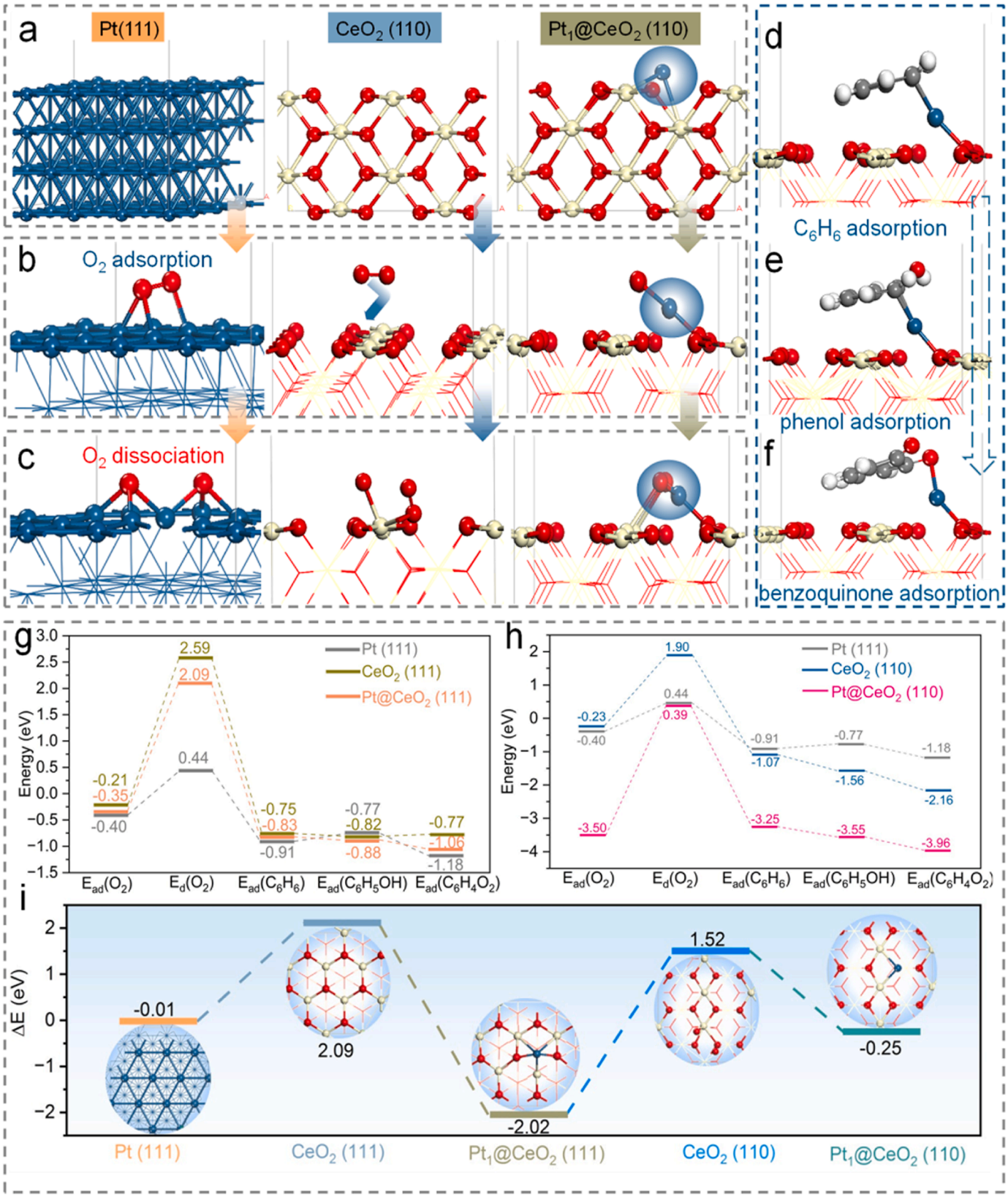

Fig. 6. DFT Calculation: (a) Side view of the optimized configurations of Pt (111), CeO_2 (110), Pt_1 @CeO_2 (110) samples, (b) the adsorption of O_2 on the surface of different samples, (c) the dissociation of O_2 on the surface of different samples, (d) the adsorption of benzene, (e) the adsorption of phenol, (f) the adsorption of benzoquinone, (g) Schematic of energy profile on Pt (111), CeO_2(111), Pt_1 @CeO_2 (111) sample, (h) Schematic of energy profile on Pt (111), CeO_2(110), Pt_1 @CeO_2 (110) sample (E_{ad}=adsorption energy, E_d=dissociation energy), and (i) Reaction heat for ring-opening of $C_6H_4O_2$ intermediate.

transformed into benzoquinone. After that, the aromatic rings of benzoquinone were disrupted to produce the maleate species. Finally, the formed maleate species were further converted with active oxygen species into the final products CO_2 and H_2O. The activation of benzene follows the route of benzene→ phenol→ benzoquinone→ maleic acid → CO_2 and H_2O.

To explore the role of oxygen vacancies in activating oxygen molecules, in situ surface enhanced Raman spectroscopy (SERS) of Pt@CeO_2 and Pt_1@CeO_2 catalysts were conducted in N_2 and 20 vol% O_2/N_2 atmosphere in Fig. 5d and e. The band at 250 cm^{-1} corresponds to the stretching mode of Pt-O_2 vibration, and the prominent band at 460 cm^{-1} is related to the Ce-O [49]. A band at 600 cm^{-1} is related to the Pt-O-Ce, and the bands in the range of 1257, 1472, and 1590 cm^{-1} are ascribed to the characteristic absorbance of benzene. For Fig. S16 and S17, we observed that the Pt_1@CeO_2 catalyst exhibited stronger adsorption capacity than that of Pt@CeO_2 catalyst. Interestingly, the Pt_1@CeO_2 sample owns the bands at 250 cm^{-1} and 600 cm^{-1} are related to the contribution of Pt-O_2 and Pt-O-Ce species, confirming that the Pt species in the Pt_1 @CeO_2 sample may exist in the form of single atom Pt. The results are consistent with EXAFS.

In addition, it is considered that benzene molecules has reacted with lattice oxygen of the Pt_1@CeO_2 sample during adsorption process, and the characteristic bands of Pt-O_2 bond at 250 cm^{-1} decrease with the increase of adsorption time in Fig. S18. These phenomena fully indicate that benzene generates a large number of intermediate species through MvK mechanism during adsorption process at 100 °C. After adsorption saturation, the 20 vol% O_2/N_2 mixed gas was introduce into the pool to react with benzene adsorbed the sample surface. According to Fig. 5c and d, it is observed that the extinction temperature of benzene characteristic peaks is about 250 °C on the Pt@CeO_2 catalyst, while the extinction temperature of benzene characteristic peaks decreases to 200 °C on the Pt_1@CeO_2 catalyst, verifying that the Pt_1@CeO_2 catalyst owns superior catalytic performance for benzene oxidation. The band of Pt-O_2 species at 250 cm^{-1} increased gradually with the increase of reaction temperature, fully verifying that MvK mechanism is followed at low temperature and the L-H mechanism is followed at high temperature. The results are consistent with in situ DRIFTS results.

Density Functional Theory (DFT) calculations were conducted to explore the interaction between oxygen, benzene, some typical intermediate species and Pt_1@CeO_2 catalyst. Classically, side view (Fig. 6a) and top view (Fig. S19-23) of the optimized configurations of Pt, CeO_2 and Pt_1@CeO_2 samples were established. The adsorption energy (E_{ad}) of oxygen, benzene, phenol and benzoquinone was calculated in Fig. 6g, h and Table S11. It is concluded that the E_{ad} order of oxygen molecular on the surface of these samples was CeO_2(111) (–0.21 eV)> CeO_2(110) (–0.23 eV)> Pt_1 @CeO_2(111) (–0.35 eV)> Pt (111) (–0.40 eV)> Pt_1 @CeO_2(110) (–3.50 eV), which means that the surface of Pt_1@CeO_2(110) was more favorable to the adsorption of oxygen molecule. The dissociation energy (E_d) of oxygen molecule on the surface of Pt_1@CeO_2(110) is the lowest, indicating oxygen molecule is more easily activated on the surface of Pt_1@CeO_2(110) catalyst. The results are in accordance with activity results. The ring-opening reaction heat ($\triangle$E) of $C_6H_5O_2$ intermediate was also calculated, and the results were exhibited in Fig. 6i. It is seen that the order of $\triangle$E for $C_6H_5O_2$ intermediate is Pt_1@CeO_2(111) (–2.02 eV)< Pt_1 @CeO_2(110) (–0.25 eV)< Pt(111) (–0.01 eV)< CeO_2(110) (1.52 eV)< CeO_2(111) (2.09 eV), verifying that the formation of Pt single atom favorably promotes the ring-opening of $C_6H_5O_2$. The above results fully indicate that the single atom Pt accelerates the adsorption and activation of oxygen molecules, and facilitates the ring-opening reaction of $C_6H_5O_2$.

4. Conclusions

In conclusion, we synthesized the atomically dispersed Pt species localized and anchored firmly into the oxygen defect of CeO_2 support by in situ domain limited encapsulation of Ce-MOFs nanocages. A series of characterizations indicate that the atomically dispersed Pt is capable of improving the catalytic activity by forming Pt-O band under the action of reducing agent. We also observed that the good water resistance may be ascribed to the confined Pt single atom into oxygen vacancies of CeO_2 support, and the PtO_x nanoparticles would be easy to aggregate deactivation under water vapor conditions. In situ DRIFTS and in situ SERS confirm that the oxygen vacancies play a key role in anchoring and forming the single atom while promoting the activation of oxygen molecule. DFT calculations also verified that the construction of single atom Pt accelerates the adsorption and activation of oxygen molecules, and facilitates the ring-opening reaction of $C_6H_5O_2$ intermediate.

Author contributions

Fang Dong and Zhicheng Tang developed the concept. Fang Dong designed these experiments and analyzed experimental data. Fang Dong, Weitong Ling, Weigao Han and Weiliang Han contributed to catalyst synthesis. Yu Meng contributed to analyse the experimental data and the theoretical calculation. Xiaona Li contributed to the in situ Raman experiments. Fang Dong and Zhicheng Tang wrote the paper. Zhicheng Tang directed the project. All the authors discussed the results and commented on the paper. All authors have given approval to the final version of the manuscript.

Declaration of Competing Interest

The authors declare that they have no known competing financial interests or personal relationships that could have appeared to influence the work reported in this paper.

Data Availability

The authors do not have permission to share data.

Acknowledgements

This work was supported by the National Natural Science Foundation of China (52070182), the DNL Cooperation Fund, CAS (DNL202004), the Joint Fund of the Yulin University and the Dalian National Laboratory for Clean Energy (YLU-DNL Fund 202206), Talents of Innovation and Entrepreneurship Project of Lanzhou, China (2022-RC-26), West Light Foundation of the Chinese Academy of Sciences, Science and Technology Program of Lanzhou City (2023-3-35), the Key Research and Development Program of Gansu Province (23YFFA0012), Province Natural Science Foundation of GanSu (23JRRA638, 23JRRA622) and Major Program of the Lanzhou Institute of Chemical Physics, CAS (No. ZYFZFX-10).

Appendix A. Supporting information

Supplementary data associated with this article can be found in the online version at doi:10.1016/j.apcatb.2024.123779.

References

[1] C. He, J. Cheng, X. Zhang, M. Douthwaite, S. Pattisson, Z. Hao, Recent advances in the catalytic oxidation of volatile organic compounds: a review based on pollutant sorts and sources, Chem. Rev. 119 (2019) 4471–4568.
[2] Z. Hou, L. Dai, J. Deng, G. Zhao, L. Jing, Y. Wang, X. Yu, R. Gao, X. Tian, H. Dai, D. Wang, Y. Liu, Electronically engineering water resistance in methane combustion with an atomically dispersed tungsten on PdO catalyst, Angew. Chem. Int. Ed. 61 (2022) e202201655.
[3] H. Zhang, G. Guo, Z. Wang, Q. He, X. He, H. Ji, Superior performance of formaldehyde complete oxidation at ambient temperature over Co single-atom catalysts, Appl. Catal. B: Environ. 333 (2023) 122774.
[4] C. Pang, R. Han, Y. Su, Y. Zheng, M. Peng, Q. Liu, Effect of the acid site in the catalytic degradation of volatile organic compounds: a review, Chem. Eng. J. 454 (2023) 140125.

[5] C. Feng, Q. Gao, G. Xiong, Y. Chen, Y. Pan, Z. Fei, Y. Li, Y. Lu, C. Liu, Y. Liu, Defect engineering technique for the fabrication of $LaCoO_3$ perovskite catalyst via urea treatment for total oxidation of propane, Appl. Catal. B: Environ. 304 (2022) 121005.

[6] J. He, X. Li, Y. Wang, J. Xiao, Y. Liu, H. Li, N. Li, Q. Xu, J. He, D. Chen, J. Lu, Ni-Mn spinel aerogel catalysts with adsorption induced superior activity for low-temperature toluene oxidation, Chem. Eng. J. 454 (2023) 140039.

[7] Y. Wang, J. He, X. Li, M. Wang, Y. Zhou, J. Xiao, D. Chen, J. Lu, Low temperature combustion of VOCs with enhanced catalytic activity over MnO_2 nanotubes loaded with Pt and Ni-Fe spinel, ACS Appl. Mater. Interfaces 13 (2021) 46830–46839.

[8] M. Xiao, X. Yu, Y. Guo, M. Ge, Boosting toluene combustion by tuning electronic metal-support interactions in in situ grown $Pt@Co_3O_4$ catalysts, Environ. Sci. Technol. 56 (2022) 1376–1385.

[9] D. Li, L. Wang, Y. Lu, H. Deng, Z. Zhang, Y. Wang, Y. Ma, T. Pan, Q. Zhao, Y. Shan, X. Shi, J. Ma, New insights into the catalytic mechanism of VOCs abatement over Pt/Beta with active sites regulated by zeolite acidity, Appl. Catal. B: Environ. 334 (2023) 122811.

[10] Z. Hou, Y. Lu, Y. Liu, N. Liu, J. Hu, L. Wei, Z. Li, X. Tian, R. Gao, X. Yu, Y. Feng, L. Wu, J. Deng, D. Wang, M. Sui, H. Dai, Y. Li, A general dual-metal nanocrystal dissociation strategy to generate robust high-temperature-stable alumina-supported single-atom catalysts, J. Am. Chem. Soc. 145 (2023) 15869–15878.

[11] K. Yang, Y. Liu, J. Deng, X. Zhao, J. Yang, Z. Han, Z. Hou, H. Dai, Three-dimensionally ordered mesoporous iron oxide-supported single-atom platinum: highly active catalysts for benzene combustion, Appl. Catal. B: Environ. 244 (2019) 650–659.

[12] A.J. Therrien, A.J.R. Hensley, M.D. Marcinkowski, R. Zhang, F.R. Lucci, B. Coughlin, A.C. Schilling, J. McEwen, E.C.H. Sykes, An atomic-scale view of single-site Pt catalysis for low-temperature CO oxidation, Nat. Catal. 1 (2018) 192–198.

[13] Y. Lu, J. Wang, L. Yu, L. Kovarik, X. Zhang, A.S. Hoffman, A. Gallo, S.R. Bare, D. Sokaras, T. Kroll, V. Dagle, H. Xin, A.M. Karim, Identification of the active complex for CO oxidation over single-atom Ir-on-$MgAl_2O_4$ catalysts, Nat. Catal. 2 (2019) 149–156.

[14] V. Muravev, G. Spezzati, Y. Su, A. Parastaev, F. Chiang, A. Longo, C. Escudero, N. Kosinov, E.J.M. Hensen, Interface dynamics of Pd-CeO_2 single-atom catalysts during CO oxidation, Nat. Catal. 4 (2021) 469–478.

[15] S. Liang, T. Zhang, Y. Zheng, T. Xue, Z. Wang, Q. Wang, H. He, Maximizing the utilization of single-atom sites on carbon-based catalysts for efficient CO_2 electroreduction with ultrahigh turnover frequency, Appl. Catal. B: Environ. 333 (2023) 122801.

[16] K. Zhang, L. Dai, Y. Liu, J. Deng, L. Jing, K. Zhang, Z. Hou, X. Zhang, J. Wang, Y. Feng, Y. Zhang, H. Dai, Insights into the active sites of chlorine-resistant Pt-based bimetallic catalysts for benzene oxidation, Appl. Catal. B: Environ. 279 (2020) 119372.

[17] S. Zhao, Y. Wei, X. Liu, X. Pen, F. Lü, F. Gao, X. Xie, C. Du, H. Yi, D. Kang, X. Tang, Formation of active oxygen species on single-atom Pt catalyst and promoted catalytic oxidation of toluene, Nano Res 13 (2020) 1544–1551.

[18] Z. Li, R. Gao, Z. Hou, X. Yu, H. Dai, J. Deng, Y. Liu, Tandem supported Pt and ZSM-5 catalyst with separated catalytic functions for promoting multicomponent VOCs oxidation, Appl. Catal. B: Environ. 339 (2023) 123131.

[19] Y. Feng, L. Wei, Y. Liu, H. Dai, Z. Zhao, J. Deng, Rapid supplement of active oxygen by constructing Pt-Fe alloy structure to improve catalytic stability for furniture paints industry VOCs removal, Sep. Purif. Technol. 324 (2023) 124621.

[20] S. Liang, T. Zhang, Y. Zheng, T. Xue, Z. Wang, Q. Wang, H. He, Single-atom catalysis of CO oxidation using Pt1/FeOx, Nat. Chem. 3 (2022) 634–641.

[21] H. Yu, W. Wang, Q. Mao, K. Deng, Z. Wang, Y. Xu, X. Li, H. Wang, L. Wang, Pt single atom captured by oxygen vacancy-rich NiCo layered double hydroxides for coupling hydrogen evolution with selective oxidation of glycerol to formate, Appl. Catal. B: Environ. 330 (2023) 122617.

[22] Z. Liu, G. Xu, L. Zeng, W. Shi, Y. Wang, Y. Sun, Y. Yu, H. He, Anchoring Pt-doped PdO nanoparticles on γ-Al_2O_3 with highly dispersed La sites to create a methane oxidation catalyst, Appl. Catal. B: Environ. 324 (2023) 122259.

[23] L. Liu, A. Corma, Metal catalysts for heterogeneous catalysis: from single atoms to nanoclusters and nanoparticles, Chem. Rev. 118 (2018) 4981–5079.

[24] H. Li, M. Wang, L. Luo, J. Zeng, Static regulation and dynamic evolution of single-atom catalysts in thermal catalytic reactions, Adv. Sci. 6 (2019) 1801471.

[25] M. Yang, S. Li, Y. Wang, J.A. Herron, Y. Xu, L.F. Allard, S. Lee, J. Huang, M. Mavrikakis, M. Flytzani-Stephanopoulos, Catalytically active Au-$O(OH)_x$-species stabilized by alkali ions on zeolites and mesoporous oxides, Science 346 (2014) 6216.

[26] M. Yang, J. Liu, S. Lee, B. Zugic, J. Huang, L.F. Allard, M. Flytzani-Stephanopoulos, A common single-site Pt(II)-$O(OH)_x$-species stabilized by sodium on "Active" and "Inert" supports catalyzes the water-gas shift reaction, J. Am. Chem. Soc. 137 (2015) 3470–3473.

[27] X. Yang, A. Wang, B. Qiao, J. Li, J. Liu, T. Zhang, Single-atom catalysts: a new frontier in heterogeneous catalysis, Acc. Chem. Res. 46 (2013) 1740–1748.

[28] M. Hatanaka, N. Takahashi, N. Takahashi, T. Tanabe, Y. Nagai, A. Suda, H. Shinjoh, Reversible changes in the Pt oxidation state and nanostructure on a ceria-based supported Pt, J. Catal. 266 (2009) 182–190.

[29] Z. Zhang, Y. Zhu, H. Asakura, B. Zhang, J. Zhang, M. Zhou, Y. Han, T. Tanaka, A. Wang, T. Zhang, N. Yan, Thermally stable single atom Pt/γ-Al_2O_3 for selective hydrogenation and CO oxidation, Nat. Commun. 8 (2017) 16100.

[30] S. Wu, H. Liu, Z. Huang, H. Xu, W. Shen, Mn1ZrxOy mixed oxides with abundant oxygen vacancies for propane catalytic oxidation: Insights into the contribution of Zr doping, Chem. Eng. J. 452 (2023) 139341.

[31] M. Ruzzi, E. Sartori, A. Moscatelli, I.V. Khudyakov, N.J. Turro, Time-resolved EPR study of singlet oxygen in the gas phase, J. Phys. Chem. A 117 (2013) 5232–5240.

[32] X. Huang, F. Dong, G. Zhang, Y. Guo, Z. Tang, A strategy for constructing highly efficient yolk-shell Ce@Mn@TiO_x catalyst with dual active sites for low-temperature selective catalytic reduction of NO with NH_3, Chem. Eng. J. 419 (2021) 129572.

[33] F. Dong, W. Han, Y. Guo, W. Han, Z. Tang, $CeCoO_x$-MNS catalyst derived from three-dimensional mesh nanosheet Co-based metal-organic frameworks for highly efficient catalytic combustion of VOCs, Chem. Eng. J. 405 (2021) 126948.

[34] X. Ma, M. Xiao, X. Yang, X. Yu, M. Ge, Boosting benzene combustion by engineering oxygen vacancy-mediated Ag/CeO_2-Co_3O_4 catalyst via interfacial electron transfer, J. Colloid Interf. Sci. 594 (2021) 882–890.

[35] L. Li, Q. Yang, D. Wang, Y. Peng, J. Yan, J. Li, J. Crittenden, Facile synthesis λ-MnO_2 spinel for highly effective catalytic oxidation of benzene, Chem. Eng. J. 421 (2021) 127828.

[36] J. Hou, J. Hu, W. Bao, J. Yao, D. Wu, J. Wang, B. Wang, Z. Zeng, X. Cui, S. Su, L. Chang, Effects of Ti modified CeCu mixed oxides on the catalytic performance and SO_2 resistance towards benzene combustion, Catal. Commun. 1742023 (2023) 106596.

[37] M. Wen, S. Song, W. Zhao, Q. Liu, J. Chen, G. Li, T. An, Atomically dispersed Pd sites on Ti-SBA-15 for efficient catalytic combustion of typical gaseous, Environ. Sci. Nano 8 (2021) 3735–3745.

[38] Y. Zhang, C. Wu, Z. Wang, J. Ji, H. Wan, W. Zou, Q. Tong, J. Sun, L. Dong, Y. Chen, Enhanced low-temperature catalytic performance for toluene combustion of CeO_2-supported Pt-Ir alloy catalysts, Appl. Surf. Sci. 580 (2022) 152278.

[39] S. Ding, C. Zhu, H. Hojo, H. Einaga, Insights into the effect of cobalt substitution into copper-manganese oxides on enhanced benzene oxidation activity, Appl. Catal. B: Environ. 323 (2023) 122099.

[40] X. Hao, L. Dai, J. Deng, Y. Liu, L. Jing, J. Wang, W. Pei, X. Zhang, Z. Hou, H. Dai, Nanotubular OMS-2 supported single-atom platinum catalysts highly active for benzene oxidation, J. Phys. Chem. C. 125 (2021) 17696–17708.

[41] W. Han, H. Zhao, F. Dong, Z. Tang, Morphology-controlled synthesis of 3D, mesoporous, rosette-like $CeCoO_x$ catalyst by pyrolysis of $Ce[Co(CN)_6]$ and applied for the catalytic combustion of toluene, Nanoscale 10 (2018) 21307–21319.

[42] H. Zhao, W. Han, Z. Tang, Tailored design of high-stability $CoMn_{1.5}O_x@TiO_2$ double-wall nanocages derived from Prussian blue analogue for catalytic combustion of o-dichlorobenzene, Appl. Catal. B: Environ. 276 (2020) 119133.

[43] G. Kyriakou, M.B. Boucher, A.D. Jewell, E.A. Lewis, T.J. Lawton, A.E. Baber, H. L. Tierney, M. Flytzani-Stephanopoulos, E.C.H. Sykes, Isolated metal atom geometries as a strategy for selective heterogeneous hydrogenations, Science 335 (2012) 1209–1212.

[44] J. Im, H. Shin, H. Jang, H. Kim, M. Choi, Maximizing the catalytic function of hydrogen spillover in platinum-encapsulated aluminosilicates with controlled nanostructures, Nat. Commun. 5 (2014) 3370.

[45] J. Jones, H. Xiong, A.T. DeLaRiva, E.J. Peterson, H. Pham, S.R. Challa, G. Qi, S. Oh, M.H. Wiebenga, X.I.P. Hernández, Y. Wang, A.K. Datye, Thermally stable single-atom platinum-on-ceria catalysts via atom trapping, Science 353 (2016) 150–154.

[46] S. Chen, L. Li, W. Hu, X. Huang, Q. Li, Y. Xu, Y. Zuo, G. Li, Anchoring high-concentration oxygen vacancies at interfaces of CeO_{2-x}/Cu toward enhanced activity for preferential CO oxidation, ACS Appl. Mater. Interfaces 7 (2015) 22999–23007.

[47] C. Dong, Z. Qu, Y. Qin, Q. Fu, H. Sun, X. Duan, Revealing the highly catalytic performance of spinel $CoMn_2O_4$ for toluene oxidation: involvement and replenishment of oxygen species using in situ designed-TP techniques, ACS Catal. 9 (2019) 6698–6710.

[48] X. Wang, Y. Liu, T. Zhang, Y. Luo, Z. Lan, K. Zhang, J. Zuo, L. Jiang, R. Wang, Geometrical-site-dependent catalytic activity of ordered mesoporous Co-based spinel for benzene oxidation: in situ DRIFTS study coupled with Raman and XAFS spectroscopy, ACS Catal. 7 (2017) 1626–1636.

[49] J. Wang, X. Shi, L. Chen, H. Li a, M. Mao, G. Zhang, H. Yi, M. Fu, D. Ye, J. Wu, Enhanced performance of low Pt loading amount on Pt-CeO_2 catalysts prepared by adsorption method for catalytic ozonation of toluene, Appl. Catal. A, Gen. 625 (2021) 118342.